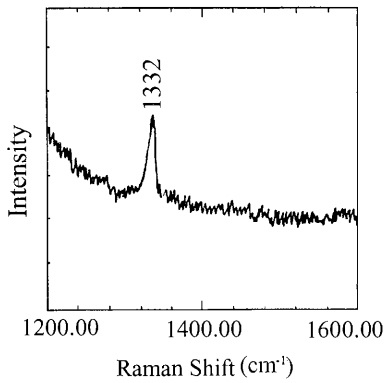

Fig. 3. Raman spectrum of sample.

resistant to acid solution. The existence of a small amount of catalyst alloy may increase the density value of the sample, whereas the amorphous carbon decreases this value. The x-ray result was consistent with the density value.

Transmission electron microscopy images and electron diffraction patterns were taken with a Hitachi H-800 transmission electron microscope. The micrograph (Fig. 2A) shows that the diamond aggregate consists of spherelike particles. Electron diffraction patterns (Fig. 2B) show two rings [(111) and (220)] of diamond and confirm the XRD result. Fig. 2C is a scanning electron microscope (SEM) image of the sample on a Ni-Co alloy plate (taken with a Hitachi X-650 SEM); this image shows that small particles are aggregated on the diamonds.

The Raman spectrum was produced at room temperature with a Spex 1403 Raman spectrometer. The Raman spectrum of the products (Fig. 3) exhibits an intense, sharp peak at 1332 cm^{-1}, indicating well-crystallized diamond.

Improvements in the process of synthesizing diamond are still needed. Much work is required to understand and control the reaction kinetics. Finding a better catalyst is very critical for the formation and growth of diamond crystal. Transitional metals (for example, Ni, Co, Mn, Fe, and Pt), their alloys, and their carbides may be the favorable catalysts (*2, 6*). In addition, substituting another halohydrocarbon carbon source (in the sp^3 hybrid state), such as C_2Cl_6, CCl_4, CBr_4, or a mixture of these, for CCl_4 may improve the process. It is reasonable to suppose that the addition of diamond seeds may increase the yield of diamond in the previously reported hydrothermal growth process (*6*). This method may provide a new means of producing diamond and other carbides, such as SiC, TiC, WC, and so forth.

References and Notes

1. J. E. Graebner, S. Jin, G. W. Kammlott, J. A. Herb, C. F. Gardinier, *Nature* **359**, 401 (1992).
2. F. P. Bundy, H. T. Hall, H. M. Strong, R. H. Wentorf, *ibid.* **176**, 51 (1955).
3. N. R. Gneiner, D. S. Phillips, J. D. Johnson, F. Volk, *ibid.* **333**, 440 (1988).
4. M. V. Thiel and F. H. Ree, *J. Appl. Phys.* **62**, 1761 (1987).
5. R. Roy, D. Ravichandran, P. Ravichandran, A. Bazian, *J. Mater. Res.* **11**, 1164 (1996).
6. X.-Z. Zhao, R. Roy, K. A. Cherian, A. Badzian, *Nature* **385**, 513 (1997).
7. W. G. Everssle, U.S. Patent 3,030,187 (1958); U. S. Patent 3,030,188 (1958); J. C. Angus, H. A. Wiu, W. S. Stanko, *J. Appl. Phys.* **39**, 2915 (1968); B. V. Spitsyn, L. L. Bouilov, B. V. Deryagin, *J. Cryst. Growth* **53**, 219 (1981); S. Mastumoto, Y. Sato, M. Kamo, N. Setaka, *Jpn. J. Appl. Phys.* **21**, L183 (1982); S. J. Harris, *Appl. Phys. Lett.* **56**, 2298 (1990).
8. A. Aisenberg and K. Chabot, *J. Appl. Phys.* **42**, 2953 (1971); E. G. Spencer, P. H. Schmidt, D. J. Joy, F. J. Sanssalone, *Appl. Phys. Lett.* **29**, 118 (1976); C. Weissmantal *et al.*, *Thin Solid Films* **72**, 19 (1980).
9. S. S. Lee, D. W. Minsek, D. J. Vestyck, P. Chen, *Science* **263**, 1596 (1994); D. S. Whitmel and R. Williamson, *Thin Solid Films* **35**, 255 (1976); L. Holland and S. M. Ojha, *ibid.* **48**, L17 (1976); M. Sokolowski, A. Sokolowska, B. Gokieli, A. Rusek, Z. Romanowski, *J. Cryst. Growth* **47**, 421 (1979); H. Vora and T. J. Moravec, *J. Appl. Phys.* **52**, 6151 (1981); K. Suzudi *et al.*, *Appl. Phys. Lett.* **50**, 728 (1987); Y. Muranaka, H. Yamashita, K. Sato, H. Miyadera, *J. Appl. Phys.* **67**, 6247 (1990); J. Lee, R. W. Collins, R. Messier, *Appl. Phys. Lett.* **70**, 1527 (1997).
10. J.-J. Wu and F. C.-N. Hong, *Appl. Phys. Lett.* **70**, 185 (1997).
11. I. L. Finar, *Organic Chemistry* (Longman, White Plains, NY, 1973), vol. 1, chap. 3, p. 76.
12. V. P. Novikov and V. P. Dymont, *Appl. Phys. Lett.* **70**, 200 (1997).
13. See supplementary x-ray data [Joint Committee on Powder Diffraction Standards (JCPDS) 6-0675].
14. S. A. Solin and A. K. Ramdas, *Phys. Rev. B* **1**, 1678 (1970).
15. We thank Y. C. Liu, H. Y. Fan, Y. H. Zhang, Q. X. Guo, and S. Q. Yu for helpful discussions. This work was supported by the National Natural Science Foundation of China and the National Nanometer Materials Climbing Project.

2 December 1997; accepted 3 June 1998

MR Imaging Contrast Enhancement Based on Intermolecular Zero Quantum Coherences

Warren S. Warren,* Sangdoo Ahn, Marlene Mescher, Michael Garwood, Kamil Ugurbil, Wolfgang Richter, Rahim R. Rizi, Jeff Hopkins, John S. Leigh

A new method for magnetic resonance imaging (MRI) based on the detection of relatively strong signal from intermolecular zero-quantum coherences (iZQCs) is reported. Such a signal would not be observable in the conventional framework of magnetic resonance; it originates in long-range dipolar couplings (10 micrometers to 1 millimeter) that are traditionally ignored. Unlike conventional MRI, where image contrast is based on variations in spin density and relaxation times (often with injected contrast agents), contrast with iZQC images comes from variations in the susceptibility over a distance dictated by gradient strength. Phantom and in vivo (rat brain) data confirm that iZQC images give contrast enhancement. This contrast might be useful in the detection of small tumors, in that susceptibility correlates with oxygen concentration and in functional MRI.

Contrast in MRI is largely based on variations in spin density or relaxation times, sometimes enhanced by injected contrast agents such as gadolinium compounds. The relation between these parameters and tissue morphology is not always unique. Thus, it is not surprising that in some applications no combination of these parameters gives sufficient useful contrast. Even with brain imaging, particularly in the rapidly expanding field of functional MRI (*1*), contrast is frequently the limiting factor. New methods for contrast enhancement could thus improve soft tissue characterization, particularly if they correlate with physiologically important characteristics.

Here, we demonstrate a type of MRI based on detection of "impossible" intermolecular multiple-quantum coherences (iMQCs) (*2–4*), specifically the zero-quantum coherences (iZQCs) (*2*) that correspond to simultaneously flipping two water spins in opposite directions on molecules separated by 10 μm to 1 mm (*3–8*). The iZQC linewidth (hence, the image contrast) is determined by local sus-

W. S. Warren and S. Ahn, Department of Chemistry, Princeton University, Princeton, NJ 08544–1009, USA. M. Mescher, M. Garwood, K. Ugurbil, Center for Magnetic Resonance Research, University of Minnesota, 385 East River Road, Minneapolis, MN 55455, USA. W. Richter, National Research Council Canada, Institute for Biodiagnostics, 435 Ellice Avenue, Winnipeg, MB R3B 1Y6, Canada. R. R. Rizi, J. Hopkins, J. S. Leigh, Department of Radiology, University of Pennsylvania, Philadelphia, PA 19104, USA.

*To whom correspondence should be addressed. E-mail: wwarren@princeton.edu

ceptibility variations, as explained below. These variations are physiologically important (for example, they are affected by tissue oxygen gradients in vivo), but are not directly measured by other imaging methods.

Many different pulse sequences are in common use in MRI experiments. A good way to understand the differences is to focus on the "prototype sequence," the pulses that actually create the spatially localized signal and contrast, and by ignoring the gradients and pulses needed for detection later. For example, the prototype sequence for a "FLASH sequence" (*9*) is a single nonselective or slice-selective low flip-angle RF pulse. If the repetition time is long compared to the relaxation time T_1, the image contrast comes essentially from variations in the bulk magnetization, which tend to be small for water imaging in living tissue. However, if the prototype sequence is a conventional spin echo (90°-τ-180°-τ), as in the spin-echo echo planar imaging (EPI) sequences used for Fig. 1A or Fig. 2A, the magnetization has additional weighting due to differences in relaxation time T_2. Other simple prototype sequences provide still other weightings; for example, delayed acquisition provides T_2^*-weighting, a FLASH sequence with a short repetition time or a preinversion pulse provides T_1-weighting, and strong gradient pairs would provide a diffusion weighting.

The sequence we used to detect an iZQC image is shown in Fig. 3. Here, the prototype sequence is essentially the HOMOGENIZED sequence (90°-gradient-τ_{zq}-45°-TE), which was shown in (*2*) to excite iZQCs. We added slice selection gradients during the pulses, a variable direction for the crosshatched "correlation gradient" in the interval labeled τ_{zq}, and one or more 180° pulses during TE. Conventional echo-planar imaging for detection follows the sequence. In the usual picture of magnetic resonance (for example, using the normal Bloch equations), the first 90° pulse converts equilibrium magnetization I_z into I_y, and the correlation gradient modulates this transverse magnetization. None of the later gradient pulses ever match this correlation gradient, so that a conventional treatment would predict no signal except from spins that relax back toward equilibrium during τ_{zq}. This treatment turns out to be incorrect—iZQC signal is detectable because of the direct dipole-dipole interaction between nuclei in solution. This interaction is conventionally assumed to be averaged away by diffusion (*10*), but this assumption is only valid for spins closer than the distance molecules diffuse on the nuclear magnetic resonance (NMR) time scale (*11*) (typically 10 μm). If the magnetization is not spatially uniform (as happens if the spins precess in a gradient), the interaction between distant spins can be quite important, and detection of intermolecular resonances is possible.

A comparison of an iZQC image of a head phantom obtained on a GE SIGNA 4-T whole body scanner with a standard EPI image (Fig. 1) shows that we can get an undistorted image with iZQCs and allows us to verify the predicted theoretical dependences, as discussed below. Figure 2 compares spin-echo EPI and iZQC images of a rat brain with a large C6 glioma (9.4-T Magnex/Varian system with an 11-cm gradient insert). It shows that the iZQC sequence generates images with fundamentally different contrast; it also presents experimentally measured "maps" of the relaxation times in different positions, showing that the decay of the iZQCs (time constant "$T_{2,zq}$") differs quite generally from T_2 or T_2^*. Decays for a few representative highlighted regions (tumor, ventricle, nontumor, and eye) are shown in Fig. 4.

Two different theoretical models can be used to explain these effects. One approach treats the couplings classically (*5, 6, 11, 12*) by modifying the Bloch equations to include the "dipolar demagnetizing field," originally introduced to explain multiple echoes in concentrated solutions (*13, 14*). A full quantum treatment (*2, 4, 14*) (that retains the dipolar couplings and discards the high-temperature approximation to the density matrix) can also be used. Both treatments make fully quantitative predictions of the signals for simple sequences (*5, 15*), but the quantum approach leads to an easier understanding of this experiment. As discussed in (*2*), the initial 90° pulse creates two-spin, intermolecular double-quantum coherences (iDQCs) and iZQCs, as well as the conventionally observed one-spin, one-quantum coherences. The correlation gradient eliminates all but the iZQCs. The second RF pulse (flip angle β) transfers iZQCs into two-spin single quantum terms such as $I_{xi}I_{zj}$. Finally, the magnetization can be rendered observable by a number of small intermolecular dipolar couplings that remove the I_z term, thus producing detectable magnetization. With uniform magnetization density, and ignoring both relaxation and inhomogeneous broadening, the exact signal at the echo time TE is

$$M^+ = iM_0 \cos\beta J_1\left(-\Delta_s \sin\beta \frac{TE}{\tau_d}\right);$$
$$\Delta_s = (3\hat{s}\cdot\hat{z})^2 - 1)/2; \tau_d = (\gamma\mu_o M_o)^{-1} \quad (1)$$

where J_1 is the first-order Bessel function; s is the direction of the gradient pulse; and τ_d is the dipolar demagnetizing time (≈230 ms for water at 4 T, ≈100 ms at 9.4 T). Because $J_1(x) \approx x/2$ for $x \ll 1$, it is initially linearly proportional to TE and grows in most rapidly for $\beta = \pi/4$ or $3\pi/4$. In this case, the predicted signal reaches a maximum of 41% of the full magnetization at TE = 2.6 τ_d.

In most realistic imaging applications, relaxation makes such a long TE impractical, and the iZQC signal is weaker than a conventional image. Susceptibility-matched head phantom images at 4 T (T_1 = 1.16 s, T_2 = 0.18 s) like those in Fig. 1B show an increase in signal intensity with TE up to 220 ms (5% of the equilibrium magnetization) followed by decreasing signal, in agreement with simulations. In addition, the iZQC-based signal is maximized experimentally when the second pulse has a tip angle of β = 45°, as expected from Eq. 1; ordinary transverse magnetization generated by the second pulse would continue to increase up to 90° and then decrease.

Because the image is weaker than a conventional image, the real utility of the iZQC images comes from contrast enhancement expected and

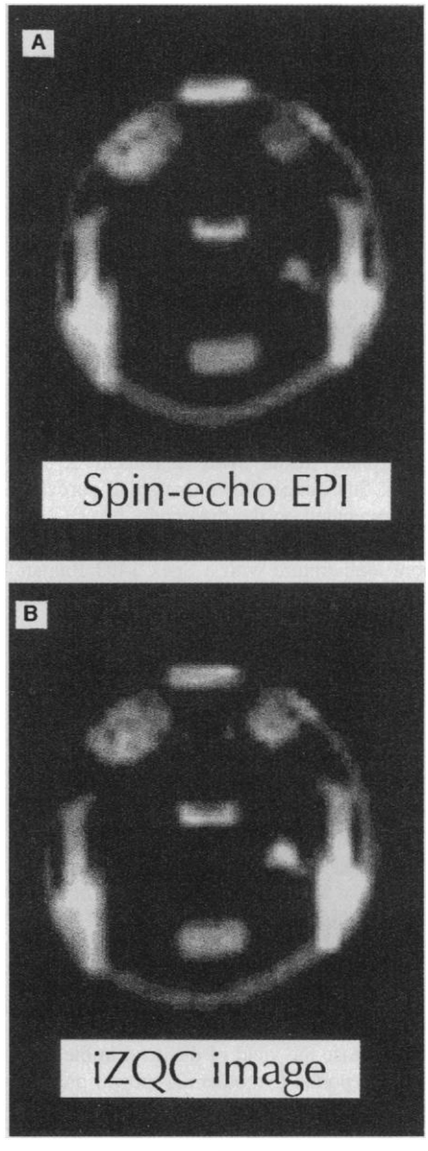

Fig. 1. Comparison of a 128 × 128 voxel standard EPI image (top, eight shots averaged) with an iZQC image (bottom, 128 shots averaged, τ_{zq} = 50 ms) for a susceptibility-matched head phantom at 4 T. In both experiments TE = 200 ms (parameters shown in Fig. 3). The signal in the iZQC experiment is about 5% of that in the conventional image.

observed in vivo (Figs. 2 and 3). To understand this contrast, note that we have previously shown (*3*) that iDQC signals come primarily from spins separated by a distance $d = \pi/(\gamma G_c t_c)$—half a cycle of the magnetization helix generated by the correlation gradient. Thus, we observed cross-peaks between coaxial tubes when the helix pitch was long (*4*). The iZQC signal has the same spatial dependence. With no inhomogeneous broadening, the iZQC decay would be exponential with decay time $T_{2,zq} = T_2/2$, since two spins participate in every iZQC. For short values of τ_{zq}, the signal is somewhat similar to a spin-echo EPI with the same echo time, because the proton density is fairly uniform; the iZQC signal ($\propto M_o^2$) exaggerates spin density variations, which probably accounts for the greater prominence of the tumor region in Fig. 2C.

However, evolution during the delay τ_{zq} (2 to 100 ms in our experiments) is affected by the resonance frequency difference on the distance scale dictated by the magnetization helix, rather than by the macroscopic inhomogeneous broadening. Significant resonance frequency variations due to the bulk magnetic susceptibility χ are expected in living tissue (*16, 17*). Well-characterized examples include lung tissue (*18*) (at the interface between air with $\chi = 0.4$ ppm and normal tissue with $\chi = -9$ ppm; 1 ppm is 170 Hz in a 4-T magnet), arterial blood vessels (different degrees of blood oxygenation on either side, changing χ by about 0.3 ppm) and sites of tissue necrosis (fully deoxygenated hemoglobin, changing χ by about 1 ppm). In conventional MRI, this variation shows up as an inhomogeneous broadening $1/T_2^*$ but iZQC detection provides a much more sensitive, and distance-selected, method for measuring these variations. For all of the experiments shown here, $d = 120$ μm, far smaller than a typical voxel size of 0.5 mm by 0.5 mm by 5 mm. At the extreme limit of inhomogeneous broadening (completely uncorrelated resonance frequencies over the distance d), if each voxel had a Gaussian decay with standard deviation T_2^*, the iZQC decay would also be Gaussian with standard deviation $T_2^*/\sqrt{2}$. In general, however, we expect the iZQC decay to be somewhere between the extreme

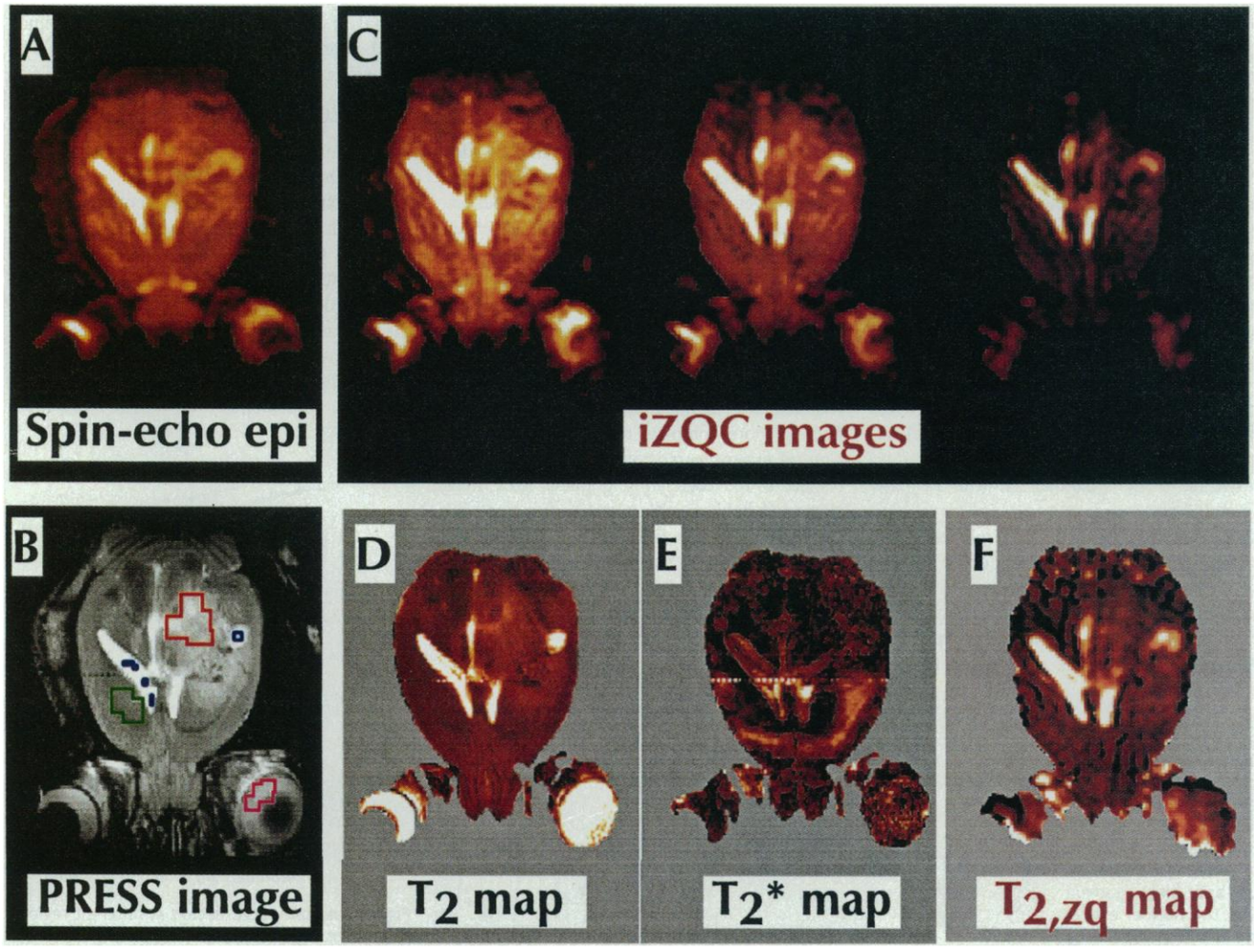

Fig. 2. (**A**) Spin-echo EPI image (two shots, four segments, 64 × 64 voxels zero-filled to 128 × 128 voxels, echo time of 50 ms) of a horizontal 5-mm slice through a rat brain at 9.4 T. (**B**) High-resolution, single-line image (PRESS image) of the same slice, highlighting regions of interest. The rat is placed prone in the magnet. The bright white line left of center is a ventricle (filled with cerebrospinal fluid) which should be matched on the right, but the right ventricle is blocked by a large tumor. The bottom of each image shows the vitreous humor in the eyes and the olfactory organ. (**C**) iZQC images with the sequence in Fig. 3 [16 shots phase cycledas described in the text, 50 ms spin-echo EPI detection as in (A)]. The three images show $\tau_{zq} = 2$, 10, and 25 ms, respectively; these images should be compared with (A). Note the contrast enhancement, higher intensity in the tumor, and variation of contrast with τ_{zq}. The signal in the 2-ms experiment is about 10% of the conventional EPI image. (**D** to **F**) Maps of relaxation times T_2, T_2^*, and $T_{2,zq}$ throughout the brain. To simplify comparison, the T_2 map is graphed on the scale (white > 100 ms, black < 20 ms); the other two maps are on the scale (white > 50 ms, black < 10 ms). Note that the images highlight different regions, implying that $T_{2,zq}$ contrast is different from conventional contrast.

homogeneous and inhomogeneous limits.

Our rat brain images show different behavior in different regions, as shown in Figs. 2 and 4. The last three pictures are not actually images, but are relaxation time "maps," where T_2 and T_2^* values are obtained from a series of high-resolution, single-line spin-echo images ("PRESS" images) (*19*), and the $T_{2,zq}$ map is obtained from a series of 11 different τ_{zq} values with 75-ms echo time. In each case, an exponential fit is assumed for each pixel to simplify comparison. The differences between these maps are striking. Figure 4 compares the decays in four fundamentally different regions, marked on the reference image in Fig. 2B. For this particular choice of parameters (75-ms echo time, d = 120 μm), we observe clean exponential decays in the tumor, nontumor, and ventricle regions. In the tumor and nontumor regions, the time constants are quite close to half of our measured values of T_2 (47.8 ± 1.8 and 36.6 ± 3 ms, respectively). Experiments varying d by a factor of 8 produced a 30% change in $T_{2,zq}$ in the tumor region, but no significant change in the nontumor region. In the ventricles, $T_{2,zq}$ decreases to 36.2 ms if the helix pitch is decreased to 60 μm, reflecting diffusional effects. Most strikingly, the decays in the eye region are highly nonexponential, much faster than homogeneous relaxation (T_2 = 102 ms) yet much slower than T_2^* relaxation (adding 5 ms to the first delay in a 50-ms PRESS sequence reduces the signal >80%). Our data thus reflect partially correlated resonance frequencies, but substantial variations in the susceptibility over short distances occur within each pixel. This decay also depends significantly on d; for d = 60 μm the decay is exponential with $T_{2,zq}$ = 16.1 ± 0.8 ms.

Susceptibility variations are refocused by the echo pulses in TE, hence that delay mainly controls the overall signal intensity and is generally optimized for TE ≈ T_2; the delay τ_{zq} is optimized instead for contrast. The ability to independently control the two delays TE and τ_{zq} to maximize signal and contrast, respectively, is a substantial advantage over iDQC imaging (*4, 8, 20*), which uses the prototype sequence 90°–t_1–{gradient}–90°–{doubled-area gradient}–t_2. That experiment only showed significant signal when the ratio of the two delays is 1:2; thus, the combination that maximizes signal (long t_2, short t_1) is not possible. However, the quantum picture makes it apparent that iDQC images could be improved simply by adding an echo (TE/2-180°-TE/2) after the delay t_2.

The quantum description that produced Eq. 1 gives us multiple ways to guarantee that the images presented here come completely from iZQCs. For example, switching between z (Δ_s = 1) and x (Δ_s = –1/2) correlation gradients multiplies the desired signal by –1/2, but leaves spurious magnetization excited by the second pulse unaffected. If the first pulse is phase shifted by 180°, the magnetization produced by the first pulse is inverted, but the iZQCs are unaffected. The iZQCs in Figs. 1, 2, and 4 come from a four-image cycle: the first pulse phase is cycled between 0° and 180° (with images added) and the gradient is cycled between z and y (with images subtracted). Stimulated echoes are eliminated by long delays between sequences (7 s) and by sandwiching a 90° pulse between a pair of magic-angle gradient pulses (x, y, and z all positive for the first pulse; x inverted for the second pulse) after each EPI sequence. The images were unchanged when the delay between sequence repetitions was dramatically changed, except for a small scaling factor reflecting more complete return to equilibrium. Control experiments showed no signal, as expected, if the correlation gradient axes were alternated between the x and y directions instead of the y and z directions, or if the second pulse was omitted. Such elaborate precautions are unnecessary for general applications; in practice, our adiabatic pulses make the phase cycling unimportant for short τ_{zq} values, and the expected –1/2 scaling after switching gradient direction is readily seen.

How can this technique be generalized? Our rat brain images with 75-ms echo time and short τ_{zq} have 10 to 15% of the EPI signal, varying somewhat by region. After two shots (phase cycling only the first pulse) the average signal to noise over the head is 16, with the pixels of greater intensity are a factor of 51 above the noise level. It would be straightforward to extend these results to multiple echoes or other detection sequences to further enhance the signal—we chose spin-echo EPI for detection here simply in order to show what was possible with very quick images. Other detection sequences might be advantageous in applications where chemical shift variations (such as water versus fat) are significant complications. Equation 1 shows that, for TE ≈ $T_2 < \tau_d$, the ratio of the iZQC signal to the full magnetization M_o depends on the concentration C, gyromagnetic ratio γ, and relaxation time T_2 as

$$(\text{iZQC signal})/M_o \propto \gamma^3 C B_o T_2 \qquad (2)$$

This result suggests that iZQC contrast enhancement is most appropriate for ^{1}H imaging. The relaxation time T_2 is generally longer at low fields (*21*), so that a wide range of field strengths (both higher and lower) should give reasonable signal strengths in optimized experiments. Also, because the iZQC signal scales as the square of the transverse magnetization, small flip-angle imaging sequences for producing the signal (such as FLASH) are not appro-

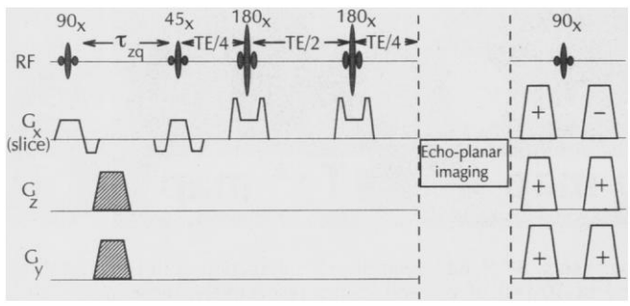

Fig. 3. Typical intermolecular zero-quantum coherence imaging pulse sequence. A standard spin-echo EPI pulse sequence was modified to include a slice-selective preparation pulse and filter gradient before the normal excitation and refocusing pulses. The filter (correlation) gradient is applied immediately after the first 90° pulse; in most of our experiments, the direction s of this gradient pulse was alternated between z and y, which multiplies the iZQC signal by –1/2 (see Eq. 1), and only a difference spectrum was retained. A slice-selective 45° RF pulse is applied after a delay τ_{zq}, and then a double-spin echo (total delay TE) allows dipolar couplings to create observable magnetization. Standard EPI gradients were used for detection. For Figs. 2 and 4, all pulses are adiabatic, to compensate for surface coil RF inhomogeneity, and the slice selection was restricted to the 180° pulses. After detection, crusher gradients were applied to suppress stimulated echoes (see text).

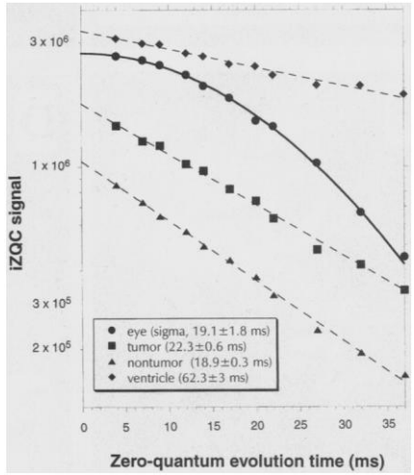

Fig. 4. Rat brain iZQC decays in different regions of interest: tumor (red box in Fig. 2B), nontumor (green box), ventricle (blue boxes), and eye (magenta box). Each data point represents four averaged images with TE = 75 ms and d = 120 μm. The noise level (rms value of data outside the image) was approximately 300 on this scale. Errors are 1σ based on quality of the fit. Note the excellent fit to single-exponential decays everywhere except in the eye, where the decay is essentially Gaussian. The functional form and decay constants change as d is varied, as discussed in text.

priate, although signal can be stored as z-magnetization and read out by a FLASH sequence.

Because the susceptibility variations measured with the iZQC method depend on local tissue oxygen concentration, in vivo this parameter varies in a much more straightforward way with tissue morphology than does the contrast in normal images. This suggests a variety of applications. Transient variations in the susceptibility are believed to be responsible for functional MRI (fMRI), and thus iZQC detection might give signal enhancements, particularly at high fields. In addition, many studies have related microvessel density to tumor growth potential, so iZQC detection may also be a method to "grade" or "stage" malignancy. Finally, numerous therapeutic approaches target angiogenic factors to control tumor growth, and this might be a way to evaluate "therapeutic response" to these agents.

References and Notes

1. R. C. McKinstry and D. A. Feinberg, *Science* **279**, 1965 (1998) and references therein.
2. S. Vathyam, S. Lee, W. S. Warren, *ibid.* **272**, 92 (1996).
3. W. S. Warren, W. Richter, A. H. Andreotti, B. T. Farmer II, *ibid.* **262**, 2005 (1993).
4. W. Richter, S. Lee, W. S. Warren, Q. He, *ibid.* **267**, 654 (1995).
5. S. Lee, W. Richter, S. Vathyam, W. S. Warren, *J. Chem. Phys.* **105**, 874 (1996).
6. W. S. Warren, S. Lee, W. Richter, S. Vathyam, *Chem. Phys. Lett.* **247**, 207 (1995).
7. P. Broekaert, A. Vlassenbroek, J. Jeener, G. Lippens, J.-M. Wieruszeski, *J. Magn. Reson. A* **120**, 97 (1996).
8. P. Robyr and R. Bowtell, *ibid.* **121**, 206 (1996); R. Bowtell and P. Robyr, *Phys. Rev. Lett.* **76**, 4971 (1996).
9. J. Frahm, A. Haase, D. Matthaei, *Magn. Reson. Med.* **3**, 321 (1986).
10. N. Bloembergen, E. M. Purcell, R. V. Pound, *Phys. Rev.* **73**, 679 (1948).
11. Q. He, W. Richter, S. Vathyam, W. S. Warren, *J. Chem. Phys.* **98**, 6779 (1993).
12. M. Levitt, *Concepts Magn. Reson.* **8**, 77 (1996).
13. G. Deville, M. Bernier, J. M. Delrieux, *Phys. Rev. B* **19**, 5666 (1979); D. Einzel, G. Eska, Y. Hirayoshi, T. Kopp, P. Wölfle, *Phys. Rev. Lett.* **53**, 2312 (1984); R. Bowtell, R. M. Bowley, P. Glover, *J. Magn. Reson.* **88**, 643 (1990); H. Körber, E. Dormann, G. Eska, *ibid.* **93**, 589 (1991); A. S. Bedford, R. Bowtell, R. M. Bowley, *ibid.*, p. 516.
14. X. Zhou, C. S. Potter, P. C. Lauturbur, *Proc. Soc. Magn. Reson. Med.* (1991), p. 345.
15. J. Jeener, A. Vlassenbroek, P. Broekaert, *J. Chem. Phys.* **103**, 1309 (1995).
16. C. S. Springer, in *NMR in Physiology and Medicine*, R. J. Gillies, Ed. (Academic Press, Orlando, FL, 1994), pp. 75–99.
17. Z. M. Bhujwalla, D. C. Shungu, Q. He, J. P. Wehrle, J. D. Glickson, in (*16*), pp. 311–328.
18. C. H. Durney *et al.*, *J. Magn. Reson.* **85**, 554 (1989).
19. D. G. Schupp, H. Merkle, J. M. Ellermann, Y. Ke, M. Garwood, *Magn. Reson. Med.* **30**, 18 (1993).
20. S. Mori, R. E. Hurd, P. C. M. van Zijl, *Magn. Reson. Med.* **37**, 336 (1997).
21. Y. Crémillieux, S. Ding, J. F. Dunn, *ibid.* **39**, 285 (1998).

22. Supported by NIH under grants GM35253 (Princeton University); RR02305 (University of Pennsylvania); and RR08079, CA64338, and the W. M. Keck Foundation (University of Minnesota). W.S.W. wishes to thank J. Videen, M. Middleton, and E. Wong (University of California San Diego) for useful discussions. The experimental data discussed here can be viewed in more detail at www.princeton.edu/~wwarren

30 June 1997; accepted 28 April 1998

Evidence for the Use of Fire at Zhoukoudian, China

Steve Weiner, Qinqi Xu, Paul Goldberg, Jinyi Liu, Ofer Bar-Yosef

Zhoukoudian is widely regarded as having the oldest reliable evidence for the controlled use of fire by humans. A reexamination of the evidence in Layer 10, the earliest archaeological horizon in the site, shows that burned and unburned bones are present in the same layer with stone tools. However, no ash or charcoal remnants could be detected. Hence, although indirect evidence for burning is present, there is no direct evidence for in situ burning.

The use of fire was an important asset for our early ancestors, offering them protection against large carnivores, warmth, added nutrition, and light at night. The ability to make and maintain fire was probably a prerequisite for occupation of the higher latitudes of Eurasia. It is therefore important to know when humans acquired this skill. Some studies suggest that the use of fire goes back more than 1 million years (*1–3*), although the evidence presented for almost all sites older than 300,000 to 400,000 years is controversial (*4*).

The oldest reliable evidence has been thought to be from Locality 1 at Zhoukoudian (Peking Man Site) (*4–6*), which accumulated from about 500,000 to 200,000 years ago (*7, 8*). Over 60 years ago, the original investigators noted in Layers 10 and 4 the presence of "the evidently burnt condition of many of the bones, antlers, horn cores and pieces of wood found in the cultural layers, [and] a direct and careful chemical test of several specimens has established the presence of free carbon in the blackened fossils and earth. The vivid yellow and red hues of the banded clays constantly associated with the black layers is also due to heating or baking of the cave's sediments" [(*9*), p. 113]. Subsequent observations of Layer 10 as well as a few reported analyses of the bones and sediments have concurred with these early observations, although some doubts have been raised (*4, 9–14*).

The cave formed as an enlargement of a vertical fault in which silty and angular rockfall accumulated. Layer 10, the lowermost archaeological horizon, is about 50 to 65 cm thick and is composed of two lithological units. The upper part is quite compact and comprises pink to reddish-yellow silty clay, locally cemented with small rock fragments. The lower part consists of yellowish-red, dark reddish-brown, and reddish-brown silts that become increasingly well bedded with depth (*15, 16*) (Fig. 1).

We examined the sediments in Layer 10 after cleaning the exposed section in 1996 and 1997. During the cleaning, we collected 42 bones of macrofauna and a considerably larger number of microfauna. Five of the macrofaunal bone fragments were uniformly black to grey in a freshly produced fracture surface; one had a turquoise hue. We extracted insoluble residues from the black bones after dissolution of the carbonated apatite by 1N hydrochloric acid (HCl) and the adhering silicate minerals by 40% hydrofluoric acid (HF) (*17*). Infrared (IR) spectra showed that the insoluble residues are all characteristic of burned bone organic matrix (Fig. 2A). Most of the remaining bones were yellow with speckled black surface coloration. Those tested produced residues with IR spectra characteristic of oxides (Fig. 2B). There was no appreciable acid-insoluble organic residue. Only seven of the bones from the microfauna were uniformly black and hence appear burned, out of a total of 278 collected. One of these was tested and confirmed as burned. Most of the bones, burned and unburned, were derived from the upper part of Layer 10. The small fragment with a distinct turquoise color was obtained from the lower part of Layer 10. None of the bones in the upper part were turquoise in color. We have reproduced this color experimentally by heating white- to yellow-colored fossil bones from Locality 1, including some from the upper part of Layer 10, to temperatures between 400° and 800°C for 2 hours. The optimal temperature is 600°C. Fresh bones turn black to grey under these conditions, and a black fossil bone from Layer 10 also turned turquoise.

The sediments of Layer 10 have often been described as ash (*6, 9, 10, 14–16*). Fresh wood ash is composed mainly of fine-grained calcite (*18*) and a minor amount (about 2% by weight) of a relatively insoluble phase. The latter is mainly an aggregate of soil-derived minerals embedded in a biologically produced amorphous matrix rich in Si, Al, Fe, and K. These have been called siliceous aggregates (*19, 20*). In prehistoric deposits con-

S. Weiner, Department of Structural Biology, Weizmann Institute of Science, Rehovot, Israel 76100. Q. Xu and J. Liu, Institute of Vertebrate Paleontology and Paleoanthropology, Academica Sinica, Post Office Box 643, Beijing 100044, People's Republic of China. P. Goldberg, Department of Archaeology, Boston University, 675 Commonwealth Avenue, Boston, MA 02215, USA. O. Bar-Yosef, Department of Anthropology, Harvard University, Cambridge, MA 02138, USA.